IEEE Access
Multidisciplinary | Rapid Review | Open Access Journal

Received August 16, 2021, accepted August 20, 2021, date of publication August 25, 2021, date of current version September 7, 2021.

Digital Object Identifier 10.1109/ACCESS.2021.3107868

Design and Implementation of a Full-Bridge LLC Converter With Wireless Power Transfer for Dual Mode Output Load

SEN-TUNG WU AND CHI-HSUAN HAN
Department of Electrical Engineering, National Formosa University, Yunlin 63201, Taiwan
Corresponding author: Sen-Tung Wu (stwu@nfu.edu.tw)

This work was supported by the Ministry of Science and Technology under Grant MOST 107-2218-E-150-002.

ABSTRACT The proposed research is to accomplish a converter for driving DC load or AC load with wireless power transfer (WPT) technique. In this novel scheme, a full-bridge LLC resonant converter is adopted to deliver the energy from the primary to the secondary side. Besides, the LLC converter has soft-switching characteristic of the switches at the primary to improve the efficiency of the converter if the switching frequency is selected appropriately. In order to achieve the feature of wireless power transfer, the WPT (transmitting/receiving) coils are utilized to replace the transformer. The leakage inductor can be treated as a resonant inductor integrated in the transmitting coil. In the output side, a sinusoidal pulse width modulation (SPWM) technique is added to generate AC voltage for specific load. In other words, the proposed converter can output DC or AC voltage by user's demand. In the end of this research, a LLC converter with WPT technique for 1kW is implemented. The experimental results and the related waveforms are also shown in the content. In this topology, the highest efficiency of DC output is 89.2%, and the highest efficiency of AC output is 82.6% respectively.

INDEX TERMS Full-bridge, LLC, wireless power transfer, SPWM.

I. INTRODUCTION

In nowadays, the wireless power transfer (WPT) applications are getting popular [1]–[3]. This novel energy transfer technology can be used in electric vehicle (EV) wireless charging systems, smart phone charging pads, and even the low-power wireless charging systems for medical sensors in human bodies. The benefits of WPT interface are list as following. 1).There is no need to connect through any cables and connectors; it helps to increase the convenience of charging. 2). No spark during the entire charging process; this can improve the safety issue of charging devices. In general, WPT techniques are often used for DC applications, such as batteries. However, for home appliances and consumer products, AC loads are quite often used in daily life as well.

In fact, most of the wireless applications powered by batteries are charged by DC power source, and the wireless battery charger needs to be designed appropriately by following the specification of the battery module. To review the development of plug-in electric vehicles charging solutions [4], the EV charging pile in the charging station with cables can be classified into AC charging and DC charging [5], [6]. In [A8], AC charging time is much longer than DC charging time. Both of them have their benefits individually, for example, DC charging time is shorter, and the charging current is higher. Thus, the cost of building and the complexity of designing a DC charging pile will be increased for sure. To consider the EV's battery system, if the EV's battery is charged by AC source, an on board charger (OBC) [7] is necessary for AC to DC conversion and charging circuits. Conversely, a DC charged EV's battery system has no OBC stage within the vehicle. These features and the related charging solutions are determined by the charging mode of EV. In recent years, the EV charging solutions have been progressed from charging piles [8], [9] to wireless charging platforms. There are many articles about EV wireless charging techniques which are investigated. In general, the wireless power transferring for magnetic field techniques can be divided into magnetic-inductive (MI) charging and magnetic-resonant (MR) charging. For MI charging, the air gap distance between the transmitting coil and the receiving coil is for several centimeters. The power transfer capability of inductive

The associate editor coordinating the review of this manuscript and approving it for publication was Yuh-Shyan Hwang.

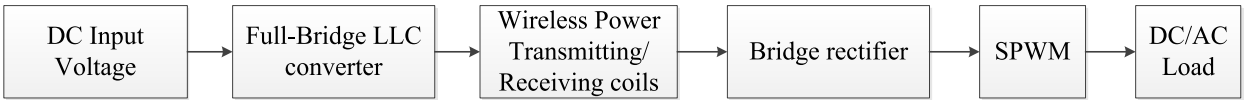

FIGURE 1. Block diagram of the proposed structure.

charging mechanism is suitable for low to medium power range (several kilowatt-scale). The cost and complexity of MI charging is lower. For MR charging, the air gap can be extended for several meters, and the power transfer capability of MR charging mechanism can reach to high power range (hundreds of kilowatt-scale) [10]. This is suitable for high power and longer air gap distance applications. However, the complexity of MR charging circuit and the resonant frequency is very high; it also shows the potential challenge and risk of EMI issues.

Wireless charging platforms and stations for EV are usually shown in parking spaces in some public areas or residential places [11]–[13]. When EV is parked in public areas such as shopping malls, rest stops, and working places, DC charging is the most popular solution for EV [14]. The reason is that DC charging speed is much faster than AC charging mode [15]. The EV users may spend a short time or even a few hours for charging their EVs by DC charging piles during the short stay. However, once the EV is charged by AC source, it will be very inconvenient for AC charged EV system to park in DC charging areas. On the other hand, if the wireless charging platforms are built for AC and DC charging modes separately. The construction cost will also be much higher [16]. Based on these reasons above, the proposed wireless power transfer circuit for dual mode is provided in this paper.

In order to satisfy the user's requirements for DC load or AC load with WPT interface, the proposed scheme utilizes two sets of the full-bridge (FB) converters. In this circuit, the FB converter with LLC resonant tank [17], [18] makes all these switches have zero-voltage-switching (ZVS) function in the primary side [19], [20]. Due to the soft-switching characteristic, the efficiency of the entire converter can be improved effectively. In this paper, the switching frequency (f_s) is designed to be vicinity of the first resonant frequency (f_r). Thus, the full-bridge LLC converter at the primary side can be operated in ZVS region for each switch when the output load varies in all loading conditions. After the energy passes through the bridge rectifier, a FB converter at the secondary side with unipolar SPWM [21]–[23] triggering mechanism can generate AC voltage with line frequency for consumer products powered by AC voltage from the proposed converter. In the content, the design consideration is being discussed. Besides that, the experimental and simulated results are also presented in the end of the paper to prove that the proposed scheme is feasible.

This study will be divided into the following parts. The proposed dual mode output structure and the operation principles are demonstrated in section II. In Section III, the design consideration of the LLC resonant tank and the WPT coils are provided. After the key components are determined, the simulation and the experimental results are shown in Section IV. In this section, the DC and AC output waveforms are simulated and measured to validate with figures. In the end of this paper, Section V will conclude the features and the future work.

II. THE OPERATION PRINCIPLES OF THE FB LLC CONVERTER WITH THE WPT COILS

The block diagram of the proposed structure is shown in Fig. 1. The input voltage is set for 155.5Vdc. The reason is that the AC main is 110Vac in some Asian local areas. The input DC voltage is fed to the full-bridge LLC converter to generate high frequency AC square voltage for triggering the resonant tank. The resonant tank helps to deliver the energy to the secondary through the WPT coils. After the bridge rectifier, the output voltage is DC, and the converter with SPWM is connected to generate line frequency (60 Hz) voltage for specific AC load. Fig. 2 shows the proposed circuit with WPT coils and the default current direction of each component.

As shown in Fig. 2, the primary side of the converter is a full-bridge scheme with LLC resonant elements (C_r, L_r, and L_m). These components help to excite the resonant tank for soft-switching function [24]. The switches in the primary side from Q_1 to Q_4 are turned on diagonally for generating high frequency AC square voltage, and the duty cycle for the each switch is about 50% approximately (with short duration dead-time). The connection between the primary and secondary side is the WPT coil to deliver the energy to the secondary through the resonant components. After the energy delivered to the secondary side, a four-diodes (from D_5 to D_8) bridge rectifier is placed to obtain a stable DC voltage. Referred to Fig. 2, the post-stage of a FB converter with SPWM technique can generate AC line voltage to the output load. On the other hand, the output load can obtain DC voltage if Q_5 and Q_8 turn on, Q_6 and Q_7 turn off all the time. That is, the output for DC or AC mode can be determined by the SPWM driven signal. The detailed operation principle is stated below.

A. OPERATION PRINCIPLE FOR DC OUTPUT LOAD

For DC load application, the diagonal switches (Q_5, Q_8) of the SPWM FB converter keep turning on to achieve a DC output function in this mode. The theoretical waveforms are shown in Fig. 3 and the detailed operation analysis is divided into the following steps below.

1). State I (t_0-t_1): This is the transferring state for negative i_{Lr} as shown in Fig. 4. When Q_2 and Q_3 are turned on, the

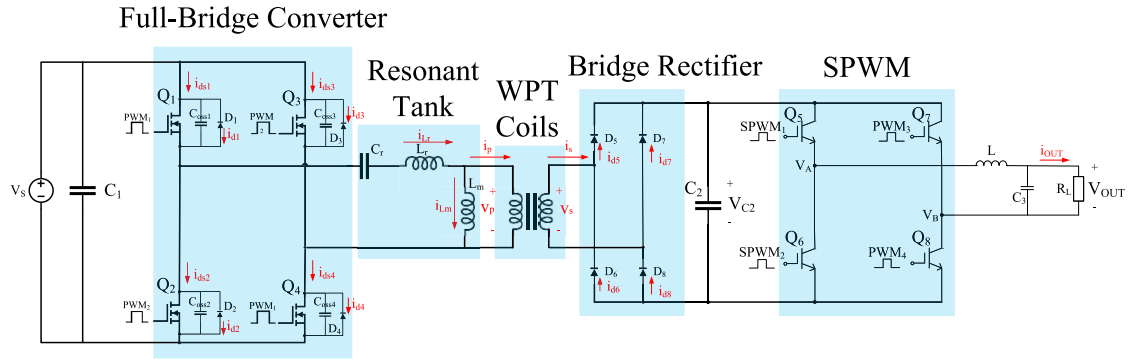

FIGURE 2. The proposed circuit with WPT coils.

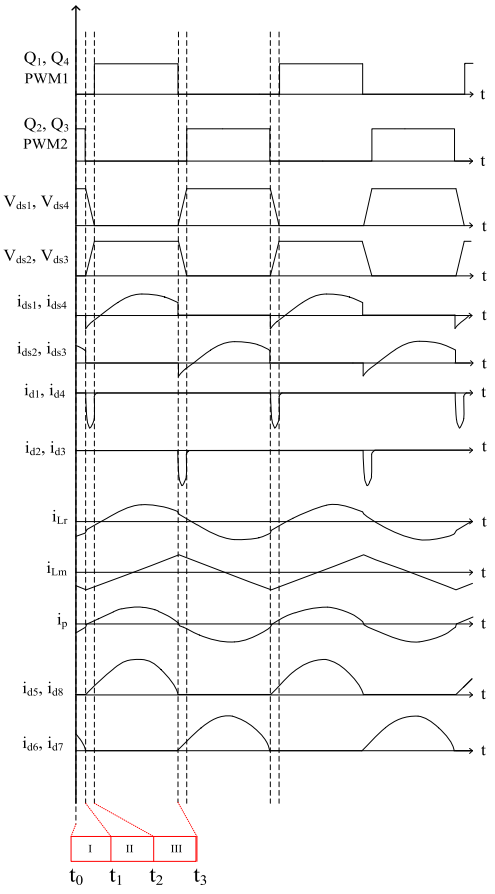

FIGURE 3. Theoretical waveforms of the proposed scheme for DC load.

input DC voltage V_s applies to the primary winding. D_6, D_7 are also turned on to deliver the energy through Q_5 and Q_8 to the output load. In this duration, the resonant current i_{Lr} which charges to L_r and C_r is equal to the sum of i_{Lm} and i_P. However, L_m is also charged by the voltage reflected from the output. At t_1, i_{Lr} is equal to i_{Lm} as i_P decreases to 0. In the secondary, i_{D6} and i_{D7} also drop to 0 when this duration ends. The resonant current is ready to commutate at the next state. In the meanwhile, the filtering capacitor C_2 provides a stable DC voltage to the output load.

2). State II (t_1-t_2): The state is the dead time duration and also the preparation for the coming commutation. As shown in Fig. 5, all the switches in the primary side are turned off. The resonant current i_{Lr} keeps flowing to provide the energy to the load continuously (D_5, D_8, Q_5, and Q_8 are also turned on to deliver the energy to the output load). When i_{Lr} is decreasing and unable to provide the energy, the WPT coils is decoupling and C_2 starts to provide the energy to the load, the current path is shown in Fig. 6. In the meantime, C_{oss1} and C_{oss4} discharge to zero through the current path. This situation helps to achieve ZVS function for the next coming state. Conversely, C_{oss2} and C_{oss3} are charged to V_s in this duration as well.

3). State III (t_2-t_3): This is the transferring state for positive i_{Lr}. When Q_1 and Q_4 are turned on with ZVS function, the input DC voltage V_s is added to the primary winding and the energy is delivered to the output load through the resonant tank (D_5, D_8, Q_5, and Q_8 are also turned on). The resonant current i_{Lr} starts to increase, and L_m is also charged by the voltage reflected from the output. Thus, i_{Lm} increases in this duration as well. At t3, i_{Lr} is equal to i_{Lm} when i_P drops to 0. The following process of the negative waveforms for i_{Lr} and i_{Lm} are the same derivations as the previous discussions. The current path is shown in Fig. 7.

B. OPERATION PRINCIPLE FOR AC OUTPUT LOAD

In this section, the post stage of the FB converter is driven by unipolar SPWM technique. Thus, the AC output voltage with line frequency (60Hz) can be obtained across the output load R_L. In theory, the voltage on the electrolyte filtering capacitor C2 can be treated as a constant DC voltage, V_{C2}. The simplified circuit is also expressed in Fig. 8.

The SPWM circuit is composed of a full-bridge inverter. The LC low pass filter is placed to reduce high frequency noise for obtaining a pure 60Hz AC voltage, V_{OUT}, at the output. In this proposed scheme, a unipolar SPWM technique is utilized to meet AC load requirement for AC mode. Q_5 and Q_6 are triggered by high frequency signal. Q_7 and Q_8

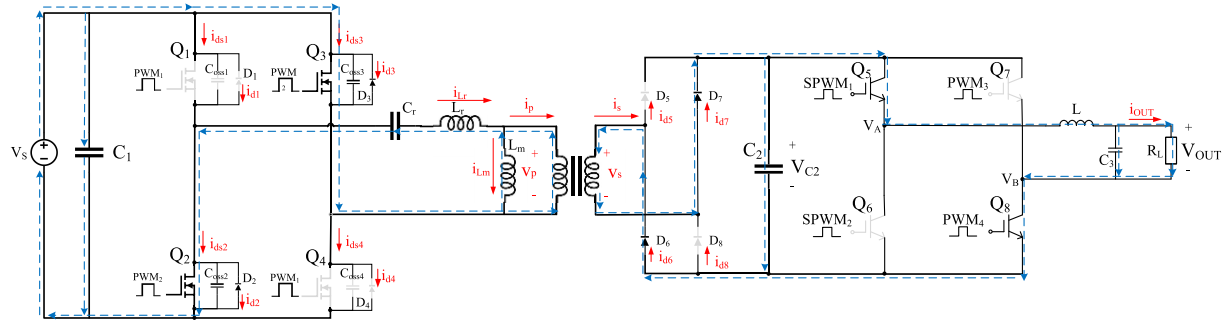

FIGURE 4. Transferring state for negative i_{Lr}.

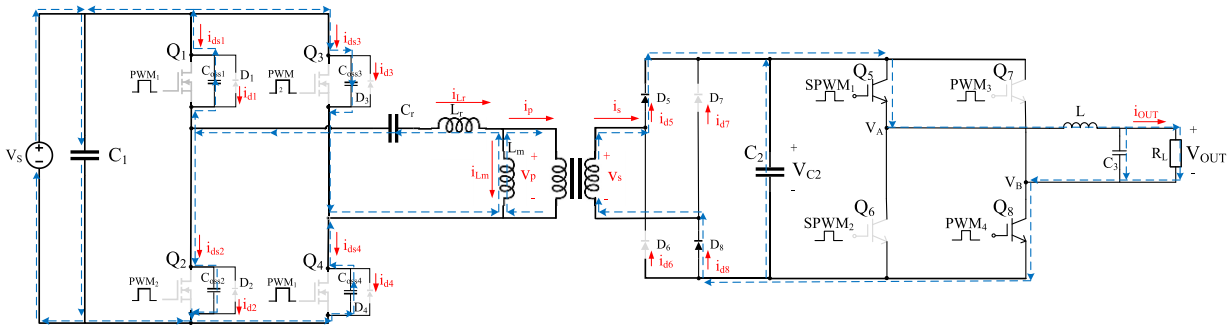

FIGURE 5. Dead time state when i_{Lr} decreases.

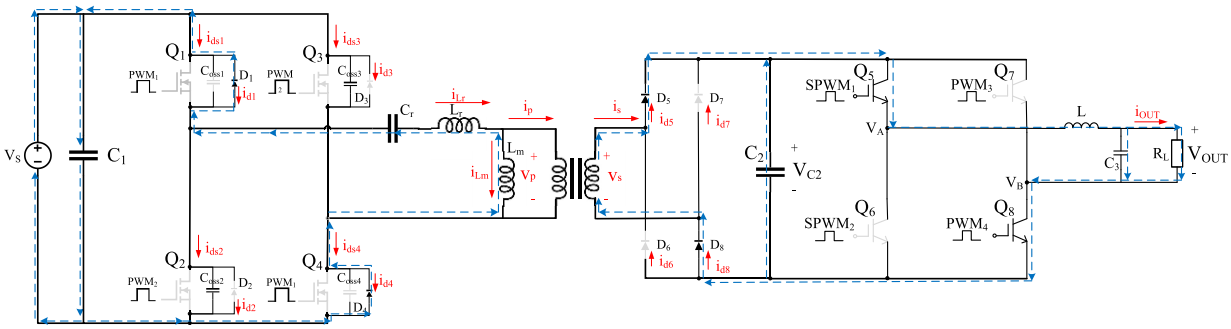

FIGURE 6. Dead time state for ZVS condition.

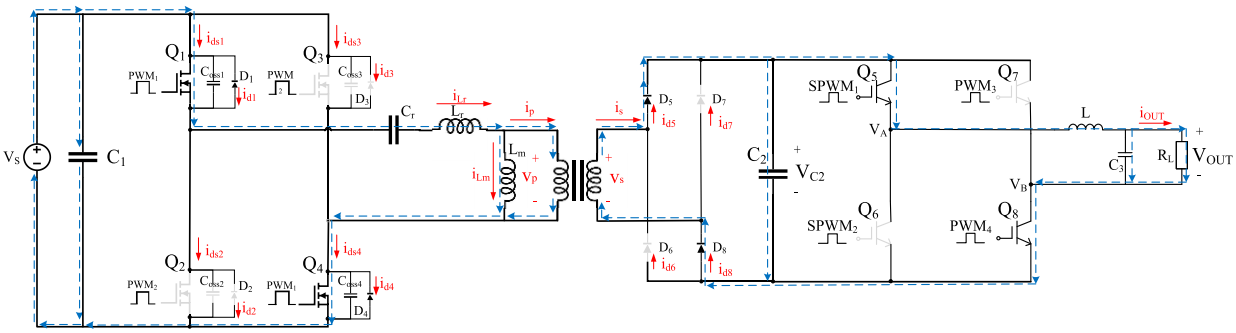

FIGURE 7. Transferring state for positive i_{Lr}.

are driven by line frequency (60Hz) signal. The theoretical waveform is shown in Fig. 9. The following ideal states will ignored the dead time durations.

1). State I (t_0-t_1): As shown in Fig. 10. When Q_5 and Q_8 turn on, Q_6 and Q_7 turn off, the terminals on V_A and V_B can be obtained. $V_A = V_{C2}$ and $V_B = 0$. Thus, V_{AB} is the

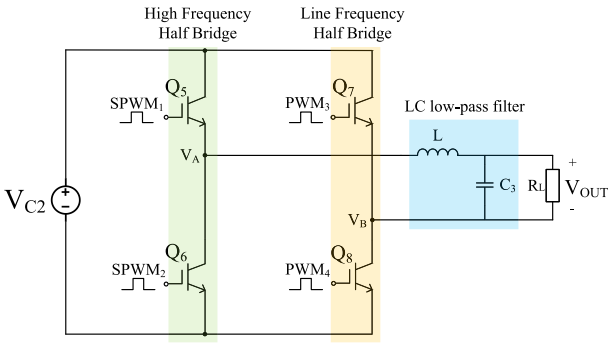

FIGURE 8. Simplified circuit for AC output load with SPWM technique.

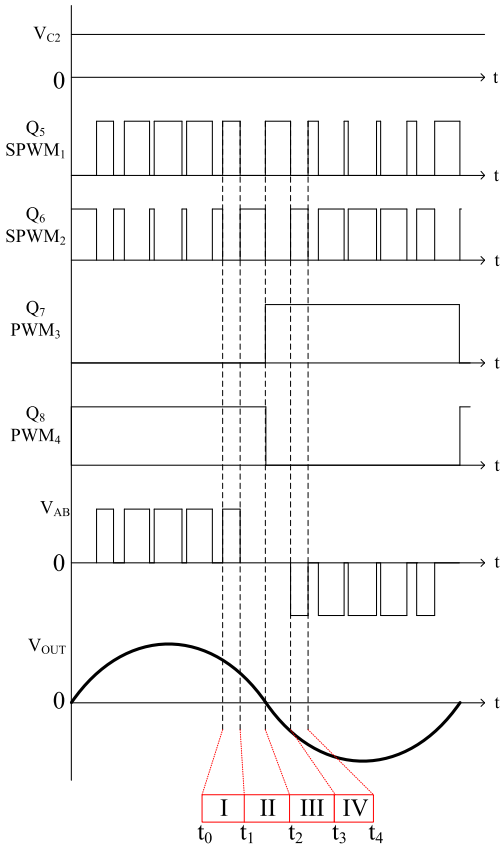

FIGURE 9. Theoretical waveforms of unipolar SPWM and AC voltage V_{out}.

input voltage V_{C2} in this state, and V_{OUT} can be determined. In this state, Q_5 is turned on with high frequency. If the turn-on duration of Q_5 is longer, V_{OUT} approaches to the positive peak easier and faster. On the other hand, if the turn-on duration of Q_5 is shorter, V_{OUT} reaches to zero faster.

2). State II (t_1-t_2): As shown in Fig. 11. When Q_6 and Q_8 turn on, Q_5 and Q_7 turn off, both of the terminals on V_A and V_B are grounded. That is, V_{AB} is 0 and the voltage across the output load V_{OUT} will decrease to 0 in the end of this state which is ready for the coming commutation.

3). State III (t_2-t_3): As shown in Fig. 12. When Q_5 and Q_7 turn on, Q_6 and Q_8 turn off. For the terminals on V_A and V_B

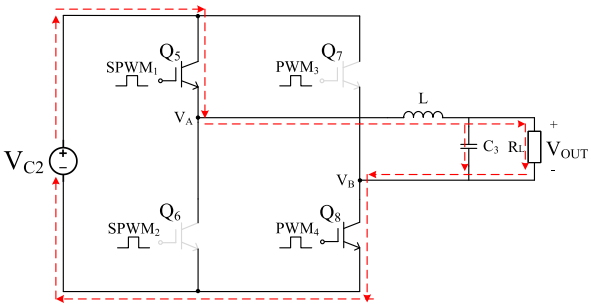

FIGURE 10. AC mode, state I (t_0 <t<t_1) for positive output voltage.

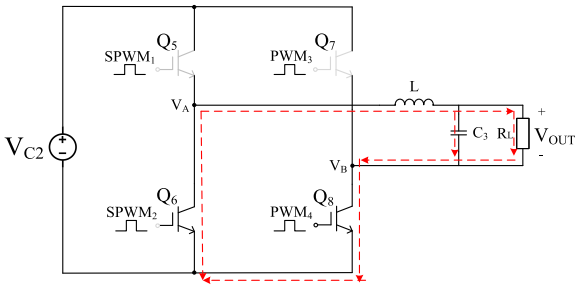

FIGURE 11. AC mode, state II (t_1 <t<t_2) for positive output voltage.

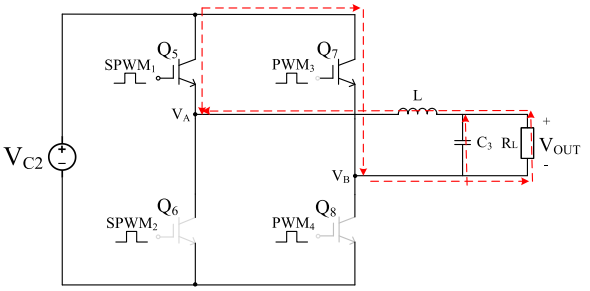

FIGURE 12. AC mode, state III (t_2 <t<t_3) for commutation to negative output voltage.

can be obtained. $V_A = V_{C2}$ and $V_B = V_{C2}$. Thus, V_{AB} is still 0 in the beginning of this state. However, the direction of the output current starts to reverse.

4). State IV (t_3-t_4): As shown in Fig. 13. When Q_6 and Q_7 turn on, Q_5 and Q_8 turn off. For the terminals on V_A and V_B, the voltage can be obtained. $V_A = 0$ and $V_B = V_{C2}$. Thus V_{AB} is $-V_{DC}$ in this state. If the turn-on duration of Q_6 is longer, V_{OUT} approaches to the negative peak easier and faster as State I.

From State I to State IV, they demonstrate an ideal concept for unipolar SPWM technique to achieve AC line voltage function across the output load.

III. DESIGN CONSIDERATION OF THE LLC RESONANT TANK AND THEWOT COILS

In order to meet the requirements and specifications of the input and the output, the LLC resonant tank [25] of the full bridge converter needs to be designed appropriately. The resonant tank in this proposed structure plays an important

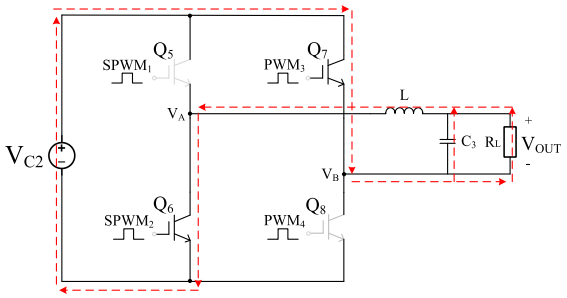

FIGURE 13. AC mode, state IV (t_3 <t<t_4) for negative output.

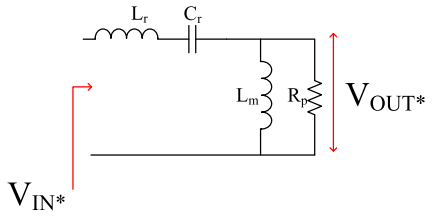

FIGURE 14. Equivalent circuit of the LLC resonant tank.

role for soft switching function. The equivalent circuit of the tank can be expressed in Fig. 14. R_P is the reflected load of the output from secondary to primary [26], [27]. In facts, R_P will vary which depends on the output loading condition.

From Fig. 14, the voltage gain M_{VR} of the resonant tank can be obtained by the following equation.

$$M_{vr} = \frac{V_{OUT*}}{V_{IN*}} = \frac{X_{Lm}//R_p}{X_{Lr} + X_{Cr} + (X_{Lm}//R_p)} \tag{1}$$

where X_{Lm}, X_{Lr}, and X_{Cr} are the impedances of L_m, L_r, and C_r. The first resonant frequency, ω_r, is determined by L_r, and C_r. The second resonant frequency, ω_m, is determined by L_m, L_r, and C_r. The quality factor Q is related L_r, C_r, and R_P. These resonant frequencies are stated below.

$$\omega_r = \frac{1}{\sqrt{L_r C_r}} \tag{2}$$

$$\omega_m = \frac{1}{\sqrt{(L_r + L_m) C_r}} \tag{3}$$

$$Q = \frac{\sqrt{\frac{L_r}{C_r}}}{R_p} \tag{4}$$

In order to normalize the transfer function with the specific parameters above, (2), (3), and (4) are substituted into equation (1) to obtain the transfer function. In this transfer function, the switching frequency $\omega_s = 2\pi f_s$. Thus, the voltage gain can be derived by using FHA method [28], [29] which is shown in equation (5).

$$M_{vr} = \frac{V_{OUT*}}{V_{IN*}} = \frac{1}{\sqrt{\left\{\frac{L_r}{L_m}\left[1 + \frac{L_m}{L_r} - \left(\frac{\omega_r}{\omega_s}\right)^2\right]\right\}^2 + \left[Q\left(\frac{\omega_s}{\omega_r} - \frac{\omega_r}{\omega_s}\right)\right]^2}} \tag{5}$$

From equation (5), the voltage gain is related to L_m, L_r, C_r and the switching frequency. Therefore, the equation (5) can be derived. In this equation, the coefficient k is the ratio of the magnetizing inductance L_m and the resonant inductance L_r($k = L_m/L_r$), the equation (5) can be rewritten as equation (6) below:

$$M_{vr} = \frac{V_{OUT*}}{V_{IN*}} = \frac{1}{\sqrt{\left\{\frac{1}{k}\left[1 + k - \left(\frac{\omega_r}{\omega_s}\right)^2\right]\right\}^2 + \left[Q\left(\frac{\omega_s}{\omega_r} - \frac{\omega_r}{\omega_s}\right)\right]^2}} \tag{6}$$

In this resonant tank, the quality factor Q is a key index to describe the sharpness of the curve and the relationship between the voltage gain and the switching frequency. If the output power increases, Q factor will also be higher. Conversely, Q will be lower when the output power drops. From Fig. 15, the higher Q represents a lower and a smoother peak of voltage gain. Fig. 15 also shows the voltage gain curves with different Q factors. The voltage gain curves can be divided into 3 regions. In order to make the switches in the primary side have ZVS function, the switching frequency (f_s) is operated between Region 2 and Region 3, these are the inductive regions. In this study, the switching frequency is operated in the vicinity of the resonant frequency.

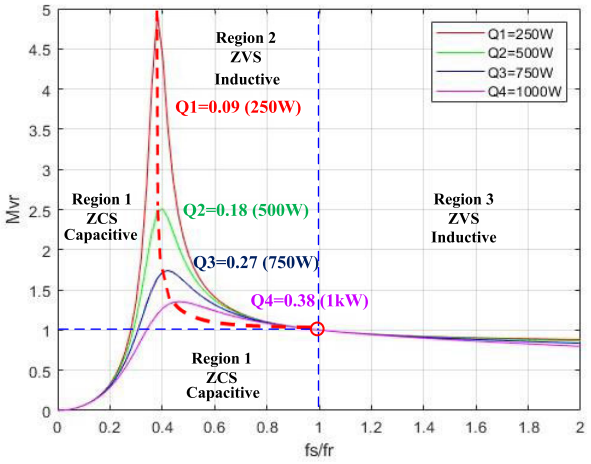

FIGURE 15. Voltage gain M_{vr} curves and normalized frequency under different load conditions (f_s: switching frequency, f_r: resonant frequency).

In this proposed research, the maximum output power is 1kW and the output voltage is set for 155.5 V_{DC} for DC output mode. Based on the specification and the different output loading conditions from Fig. 15, the designed voltage gain M_{vr} is set for 1 as the red circle shows in this figure. The reason of designed consideration is that all the curves with different loading conditions will pass through the point of unity gain; thus, the switching frequency (f_s) and the resonant frequency (f_r) are identical. To consider the non-ideal characteristic of the components and influence of the parasitic elements, the switching frequency is designed

in the vicinity of the resonant frequency for satisfying the requirements of unity gain and ZVS function. The following steps are discussed for determining the components of the resonant tank.

A. DETERMINE THE INPUT/OUTPUT VOLTAGE AND THE RANGE OF VOLTAGE GAIN

According to the application of the proposed scheme, both of the input voltage and the output voltage are set for $155.5V_{dc}$. To consider the voltage regulation at the output, the voltage gain is set abound 1 for the purpose of the output voltage regulation. The tolerance of voltage gain is designed for 10%. That is, the voltage regulation range is followed by equation below.

$$0.9 \leq M_{vr} \leq 1.1 \tag{7}$$

B. DETERMINE THE TURN RATIO OF THE WPT COILS

After setting up the voltage gain, the turn ratio of WPT coils is needed to reflect the output load from the secondary to the primary for establishing the resonant tank. As shown in Fig. 16, the cut-in voltage (1.5V) of each diode from the bridge rectifier has to be considered. The turn ratio can be obtained by the following equation. In order to meet the maximum range of the voltage regulation, M_{vr} is set for 1.1 to substitute into equation (7). Thus, the turn ratio is 1.08 by calculation. In simplification, the turn ratio (N) is chosen for 1.1 from equation (8).

$$\begin{aligned} N &= \frac{N_p}{N_s} = \frac{V_p}{V_s} = \frac{V_{IN} * \times M_{vr}}{V_{OUT} + 2V_F} \\ &= \frac{155.5 \times 1.1}{155.5 + 2 \times (1.5)} = 1.08 \cong 1.1 \end{aligned} \tag{8}$$

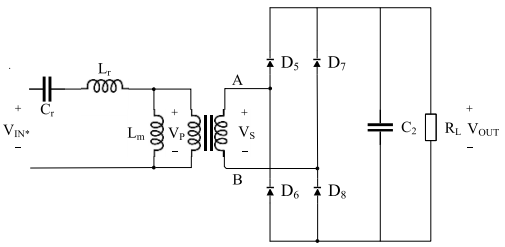

FIGURE 16. Simplified circuit for determining the turn ratio.

The equivalent resistance of R_{AB} (point A and point B are denoted in Fig. 16) at the secondary side can be calculated by equation (8). For the maximum output loading condition, $P_{OUT} = 1kW$, $V_{OUT} = 155.5V_{dc}$, and $R_L = 19.75\Omega$. These parameters are substituted into (8) to obtain R_P in (9).

$$R_P = N^2 R_{AB} = N^2 \frac{8}{\pi^2} R_L = 23.89\ \Omega \tag{9}$$

C. DETERMINE THE APPROPRIATE "k" AND "Q" FOR THE RESONANT COMPONENTS

In order to determine the appropriate ratio of the inductance k and the Q factor, in facts, lower k value brings higher voltage gain for better and more flexible regulation with narrow frequency range, but lower L_m also causes higher circulating current to increase conduction losses. Conversely, higher k value causes lower circulating current to improve the conduction losses for better conversion efficiency; however, the output voltage regulation is limited and influenced because of the smoother voltage gain curve. Based on these reasons above, k and Q have to be designed appropriately. Therefore, the variable control method is utilized from [30]. This is a proper method to find out the suitable parameters of the resonant tank. At first, the output power of the proposed converter is set for 1kW. Referred to Fig. 15, Q is obtained for 0.38 under full load condition from the calculation. By using MATLAB simulation, there are five M_{vr} gain curves can be drawn with the varying k from 2 to 10. As mentioned before, higher k has smoother and flatter gain curve, so the output voltage regulation range is limited. However, lower k has wider voltage regulation range, but the circulating current will also be higher to increase the conduction loss at the primary side. To sum up the reasons above and the design consideration of the specification, $k = 6$ is the most suitable for the proposed scheme as shown in Fig. 17.

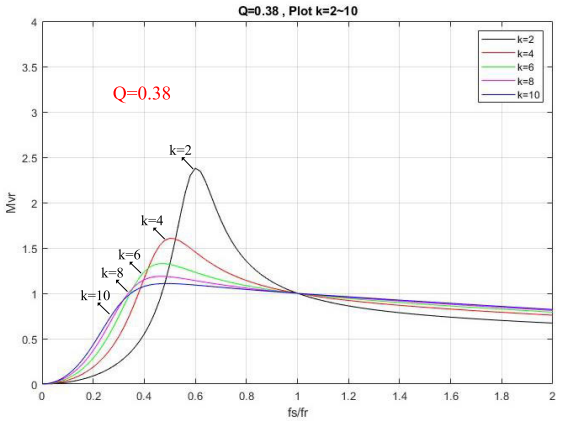

FIGURE 17. Voltage gain curves with varying k value.

After the key factors $Q = 0.38$ and $k = 6$ are determined, the gain curve is selected for the appropriate switching frequency range consequently. As shown in Fig. 18, when M_{vr} reaches to 1.1, the switching frequency decreases to $0.76 \times f_r$ if the output voltage drops. On the other hand, when M_{vr} drops to 0.9, the switching frequency will increases to $1.36 \times f_r$ if the output voltage increases. The resonant frequency (f_r) is set for 100kHz. Therefore, the proper switching frequency range with the regulated output voltage can be determined as well. By using the equation (7), (8), and (9), the key components of the resonant tank can be calculated as following.

$$\begin{aligned} C_r &= \frac{1}{2\pi \times f_r \times Q \times R_P} \\ &= \frac{1}{2\pi \times 100 \times 10^3 \times 0.4 \times 23.89} \\ &= 166.55nF \cong 167\ nF \end{aligned} \tag{10}$$

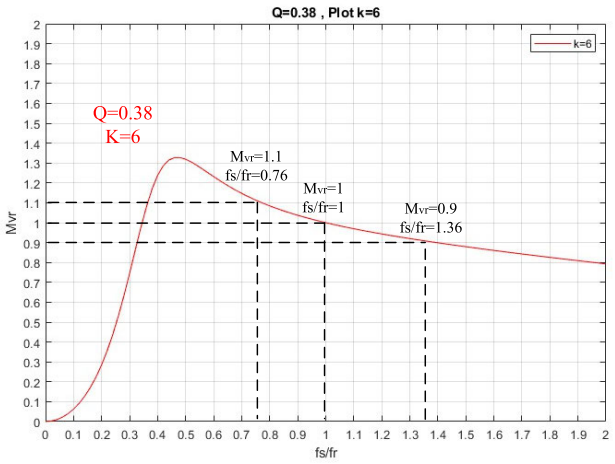

FIGURE 18. Voltage gain curve with varying switching frequency range.

$$L_r = \frac{Q \times R_P}{2\pi \times f_r} = \frac{0.4 \times 23.89}{2\pi \times 100 \times 10^3} \cong 15.2\mu H \quad (11)$$

$$L_m = k \times L_r = 6 \times 15.2\mu = 91.2\mu H \quad (12)$$

D. DESIGN AND IMPLEMENTATION OF THE WIRELESS TRANSMITTING AND RECEIVING COILS

In this section, the design of the transmitting and receiving coils are implemented. There are several things need to be considered. 1). To avoid the skin effect of the copper wire, Litz wire is adopted for reducing the impact of high frequency current, like thermal and conductivity issues. 2). Rated current from the transmitting and receiving coils are important to determine the diameter of the wire. 3). Tightness of the hand-wound coils will influence the leakage inductance easily. Based on these reasons above, the wireless transmitting and receiving coils have to be made with care for lower the leakage inductance.

1) DETERMINE THE DIAMETER OF WIRE

In general, the diameter of the wire can be selected for smaller than two times for the thickness of the skin depth, δ [31], [32]. This design guideline can improve the skin effect efficiently. By using the equation (13), the diameter can be determined with 100 kHz switching frequency. Thus, the skin depth is 0.2mm, and the suitable diameter of copper wire is lower than 0.4mm.

$$\delta = \sqrt{\frac{2\rho}{\omega\mu}} = \frac{65.6}{\sqrt{100 \times 10^3}} = 0.2mm \quad (13)$$

In equation (10), ρ is the resistivity of wire (for copper wire: $1.7 \times 10^{-8}\Omega$·m), ω is the angular frequency ($\omega : 2\pi \times$ switching frequency), and μ is permeability (μ: $\mu_0\mu_r$, where μ_0 is free space permeability ➜ $4\pi \times 10^{-7}$H/m. μ_r is relative permeability ➜ for copper: 1.26×10^{-6}H/m).

2) CONSIDEARTION OF RATED CURRENT

In this study, the diameter is set for 0.361mm which is for AWG #27 (AWG, American Wire Gauge). The maximum current of AWG #27 is 0.46A for the hand-wound WPT coils. To consider the rated current value, the output current will reach to 6.4A for full load condition. Therefore, the tolerance of the rated current is set for about twice of the output current. According to the standard of AWG and the tolerance of current, AWG #27 with 30 multi-core Litz wire ($0.46A*30 = 13.8A$) is appropriate for this WPT coil design.

3) TURNS OF HAND-WOUND WPT COILS

For conventional WPT coils winding methods, trial and error techniques are commonly used for hand-wound magnetic components, but this method will take so much wastage of wire and time wasting, especially for spiral disk coils structure. In this study, equation (14) from [33] shows that the dimension and the turns of the WPT coil are adjustable for obtaining the designed magnetizing inductance.

$$L_m = \frac{r^2 \times N^2}{8r + 11w} \quad (14)$$

In order to determine the turns of the WPT coils, this equation above helps to calculate the turn number efficiently. The parameters shown in equation (12) can refer to Fig. 19. Where r is average radius of winding in inches, and w is width of winding (in inches). All the parameters can be substituted into equation (14). For practical WPT coil, the turn number N is 31 which meet the inductance of L_m from the result of equation (12).

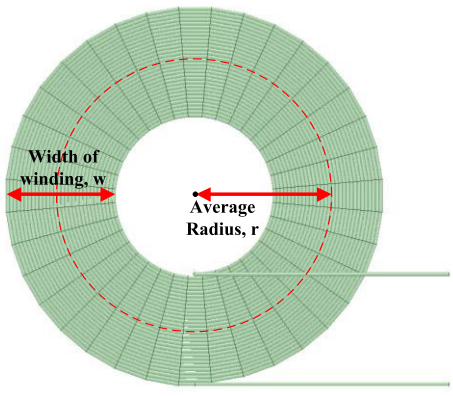

FIGURE 19. Simulated WPT coil diagram.

IV. SIMULATION AND EXPERIMENTAL RESULTS

To prove the scheme can be worked, the simulation and the experimental results are presented and listed to verify the proposed topology is feasible and implemented. The specification of the proposed topology will also be stated clearly. Besides, the efficiency for AC and DC output mode are measured and compared respectively.

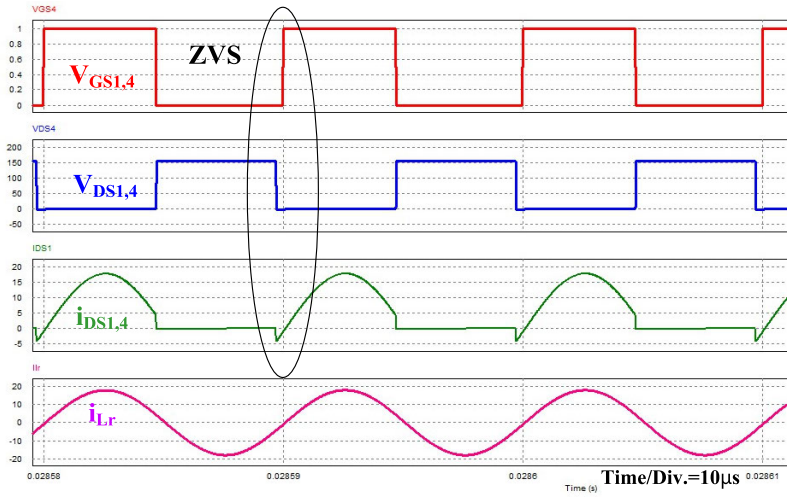

FIGURE 20. The simulated voltage and current waveforms with ZVS function under full load condition.

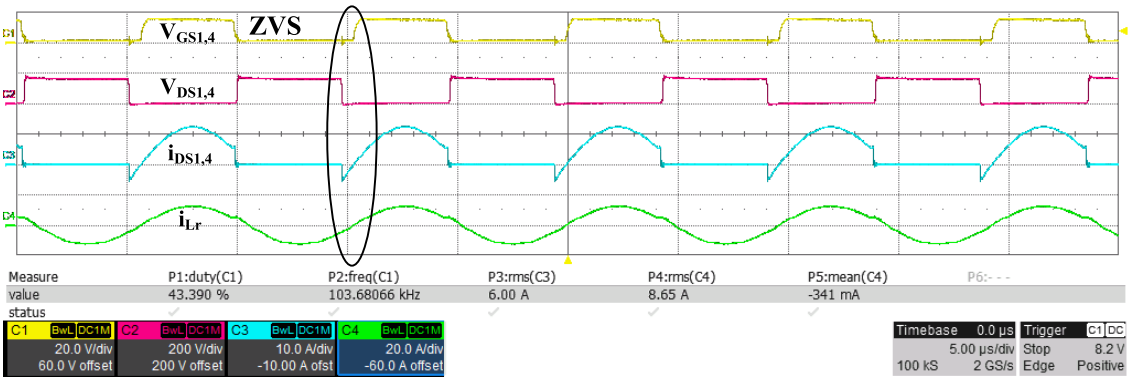

FIGURE 21. The measured voltage and current waveforms with ZVS function under full load condition.

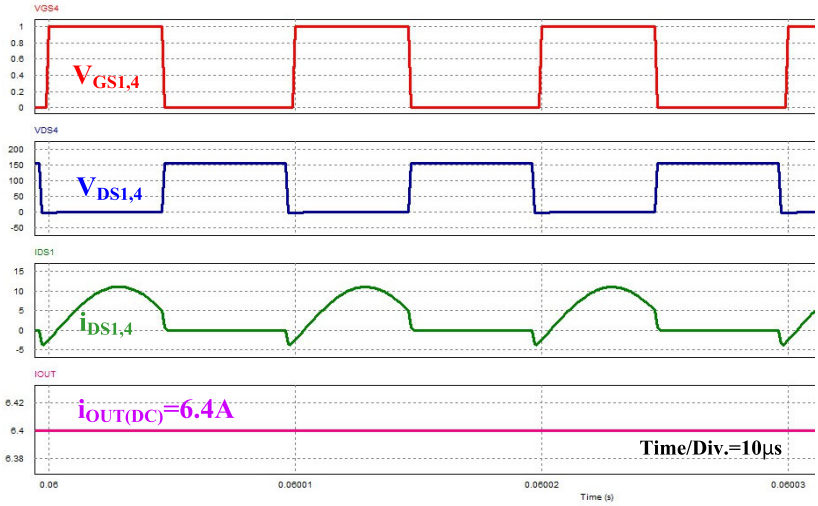

FIGURE 22. The simulated DC output voltage (154.5V) with related waveforms under full load condition.

A. SPECIFICATIONS OF THE PROPOSED SCHEME

The proposed converter is to give a novel concept that the output can generate AC or DC output for specific load through wireless interface. The input is set for 110Vac in local area. For AC mode, the output is for 110Vac. For DC mode, the output is set for 155.5Vdc. The DC output voltage

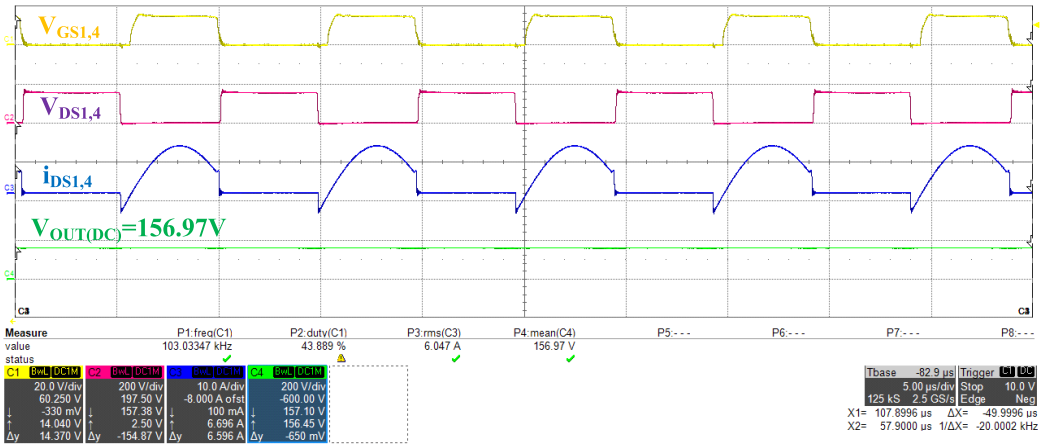

FIGURE 23. The measured DC output voltage (156.97V) with related waveforms under full load condition.

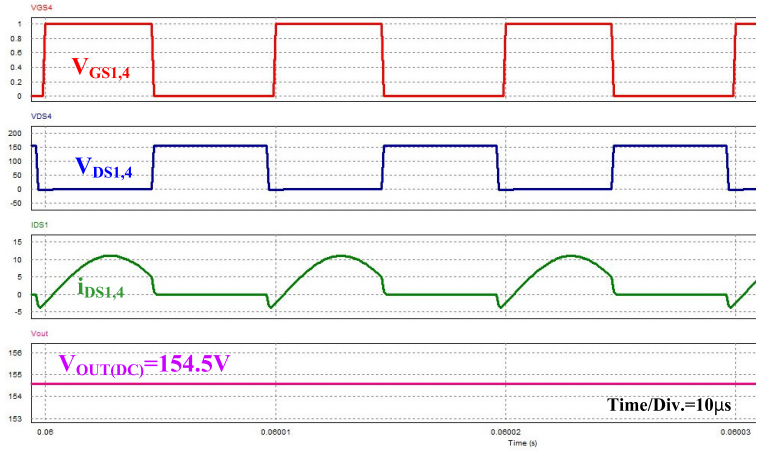

FIGURE 24. The simulated DC output current (6.4A) with related waveforms under full load condition.

TABLE 1. Specifications of the proposed converter.

Specification	Symbol	Parameter
1. DC input voltage	V_S	$155.5V_{DC}$
2. AC output voltage	$V_{OUT(AC)}$	$110V_{AC}$, 60Hz
3. DC output voltage	$V_{OUT(DC)}$	$155.5V_{DC}$
4. AC output full load	$P_{OUT(AC)}$	1kW
5. DC output full load	$P_{OUT(DC)}$	1kW
6. Resonant frequency	f_r	100kHz
7. Switching frequency	f_s	100kHz

TABLE 2. Description and symbol of components.

Description	Symbol
1. Power switch in the primary side	Q_1~Q_4
2. Power switch in the secondary side	Q_5~Q_8
3. Bridge rectifier	D_5~D_8
4. Filtering capacitor	C_1~C_3
5. Parasitic capacitor of Q_1~Q_4	C_{oss1}~C_{oss4}
6. Resonant capacitor	C_r
7. Resonant inductor	L_r
8. Magnetizing inductor	L_m
9. Current of the resonant inductor	i_{Lr}
10. Current of the magnetizing inductor	i_{Lm}
11. Current through the power switch	i_{ds1}~i_{ds4}
12. Current through the body diode	i_{d1}~i_{d4}
13. Current of the diodes in secondary	i_{d5}~i_{d8}
14. Current through the primary	i_p
15. Current through the secondary	i_s
16. Voltage of the primary	V_P
17. Voltage of the secondary	V_S
18. Output current	i_{OUT}
19. Output voltage	V_{OUT}

comes from the rectifier at the secondary. The proposed structure gives a novel idea to provide AC or DC output for specific applications. The output load is set for 1kW with AC or DC output mode. The specification is summarized in Table 1. Also, the list of the components is stated clearly in Table 2.

B. SOFT SWITCHING VERIFIED BY THE SIMULATION AND EXPERIMENTAL RESULTS

In order to prove that the proposed topology is feasible, simulation by SIMPLIS is a basic way to verify the proposed concept. As shown in Fig. 20, the primary switches are operated in ZVS under full load condition. From Fig. 20, the negative current $i_{DS1,4}$ flows through the body diode of

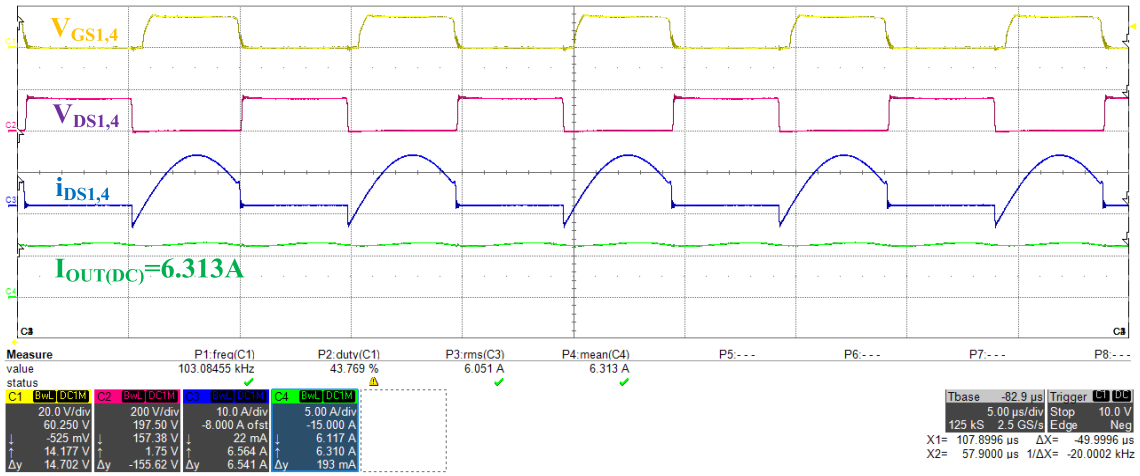

FIGURE 25. The measured DC output current (6.313A) with related waveforms under full load condition.

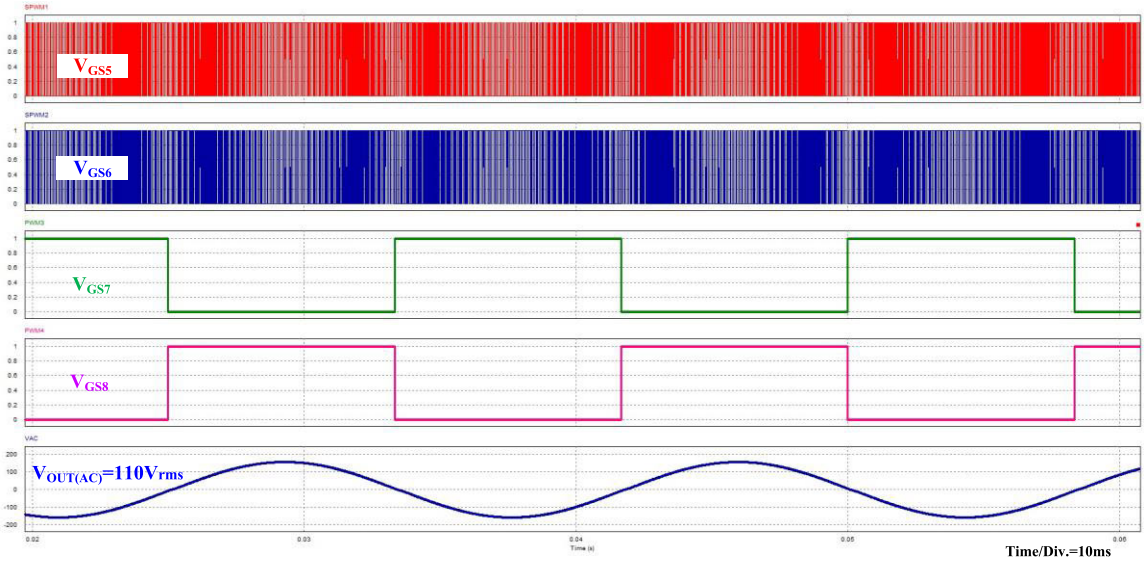

FIGURE 26. The simulated AC output voltage with related waveforms.

the Q_1 and Q_4, and $V_{DS1,4}$ drop to 0V. Then, Q_1 and Q_4 are turned on when $V_{DS1,4}$ remain 0V. Therefore, ZVS function is achieved for saving the turn-on switching loss.

From Fig. 21, this shows the experimental voltage and current waveforms for the switches at the primary side, and these four switches at the primary side achieve ZVS function successfully. The negative current $i_{DS1,4}$ flow through their body diodes to cause the low crossing voltage on $V_{DS1,4}$, then $V_{GS1,4}$ turn to high level for turning on Q_1 and Q_4. The resonant current i_{Lr} flows into the transmitting coil for delivering the energy to the receiving coil.

C. VERIFICATION OF DC OUTPUT MODE BY THE SIMULATION AND EXPERIMENTAL RESULTS

To obtain the DC output voltage from the proposed WPT topology, the diagnostic switches Q_5 and Q_8 at the secondary side need to be turned on all the time for this DC output mode. The following figures and waveforms from Fig. 22 to Fig. 25 are shown to prove the function and the concept are reasonable and feasible.

D. VERIFICATION OF AC OUTPUT MODE BY THE SIMULATION AND EXPERIMENTAL RESULTS

In this section, for gaining the AC output voltage from the proposed WPT topology, the AC output can be obtained by using SPWM technique to turn on Q_5 to Q_8 with high frequency and line frequency trigger signals. In this mode, Q_5 and Q_6 are driven by high frequency signal; Q_7 and Q_8 are driven by line frequency (60Hz) signal. The following figures and waveforms from Fig. 26 to Fig. 30 are shown to prove the function and the concept are reasonable and feasible.

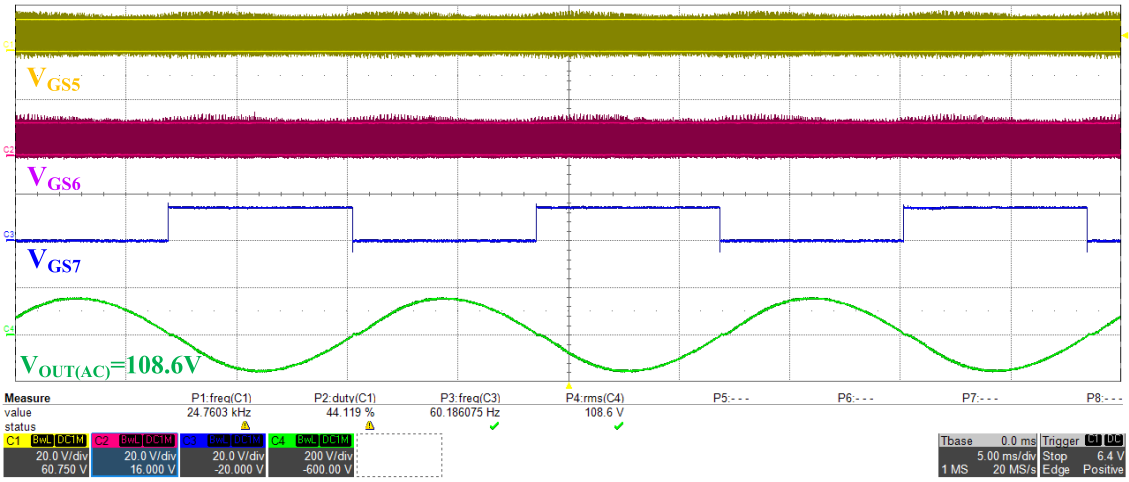

FIGURE 27. The measured AC output voltage under full load condition.

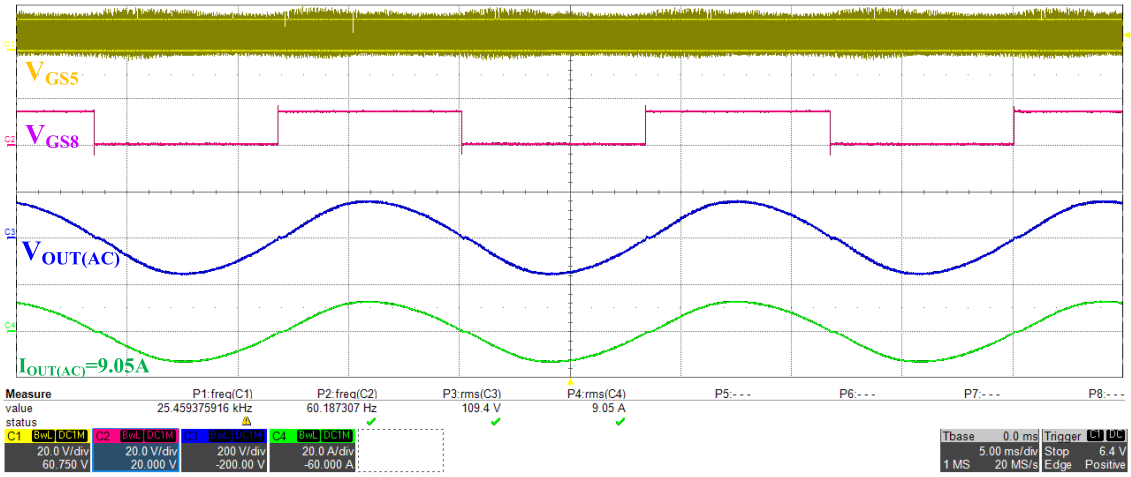

FIGURE 28. The measured AC output voltage and current under full load condition.

E. THE EFFICIENCY OF THE PROPOSED WPT CONVERTER FOR AC AND DC OUTPUT MODE

In this section, for gaining the AC output voltage from the proposed WPT topology. The AC output can be obtained by using SPWM technique to turn on Q_5 to Q_8 with high frequency and line frequency trigger signals. Q_5 and Q_6 are driven by high frequency signal; Q_7 and Q_8 are driven by line frequency signal. The following figures and waveforms are shown to prove the function and the concept are reasonable and feasible.

Referred to the efficiency curves in Fig. 31, the efficiency of AC output mode is lower than DC mode for sure. The reason is that the SPWM stage operated in AC mode with four switches takes more power losses than DC mode. To sum up the measurements, for DC output mode, the highest efficiency is 89.2%, and the average efficiency goes to 86.0%. For AC output mode, the highest efficiency is 82.6%, and the average efficiency goes to 80.0%. The experimental results show the proposed structure is feasible.

TABLE 3. Testing equipment and instruments.

Equipment and specification	Model_number
1. DC power source, (600V,8A,1.2kW)	Chroma_62024P-600-8
2. DC electronic load, (500V,50A,2.6kW)	Chroma_63202
3. Oscillation scope, (4Ch, 200MHz)	Lecroy_HDO4034
4. Voltage probe, (1.5kV,100MHz)	CYBERTEK_DP6150A
5. Current probe, (30A, 50MHz)	CYBERTEK_CP8030A
6. Digital multi-meter, (AC/DC, 10A, 1kV)	FLUKE_18B

F. PRACTICAL EXPERIMENT SETUP FOR THE PROPOSED WPT CONVERTER

The following figures from Fig. 32 and Fig. 33 provide the prototype of the circuit, the connection of testing environments, and the setup of the proposed topology. For measuring

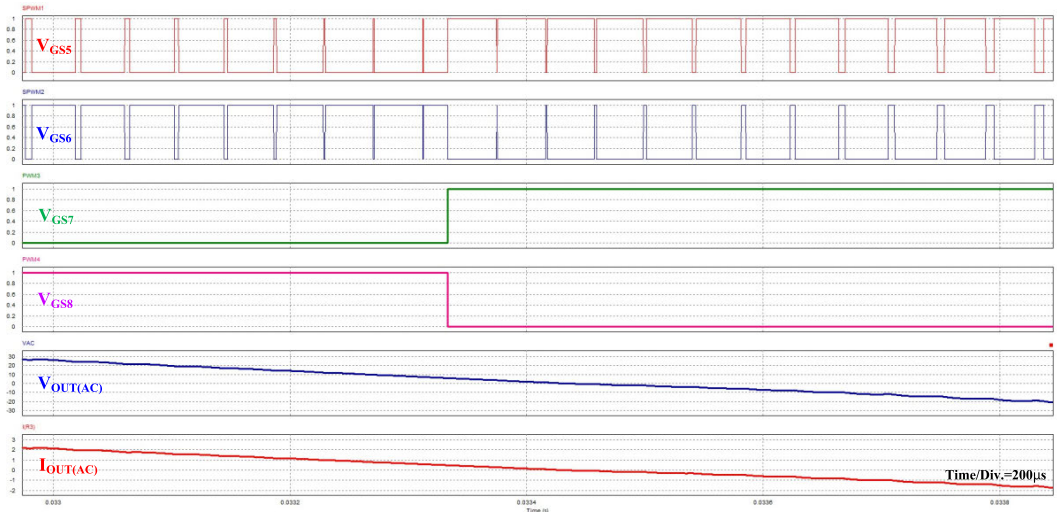

FIGURE 29. The simulated AC output voltage and current during commutation under full load condition.

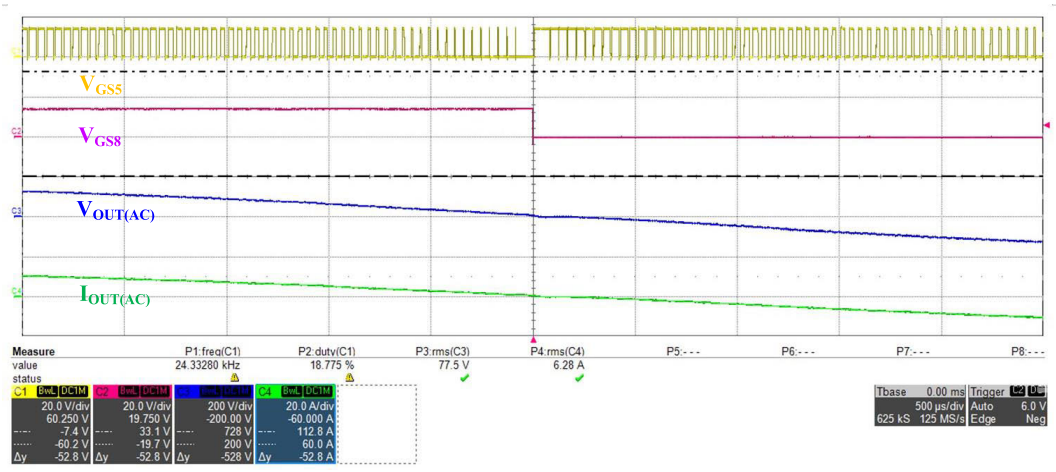

FIGURE 30. The measured AC output voltage and current during commutation under full load condition.

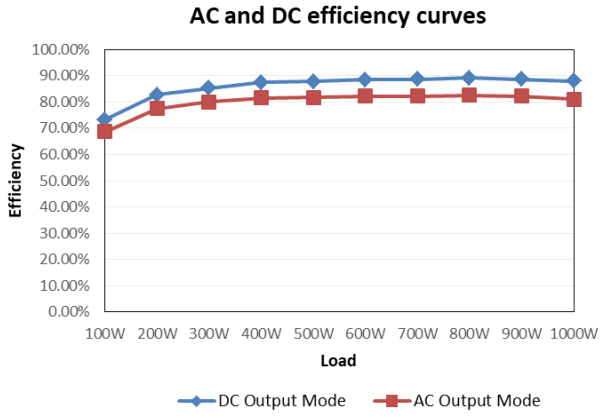

FIGURE 31. The efficiency curves between AC and DC output modes.

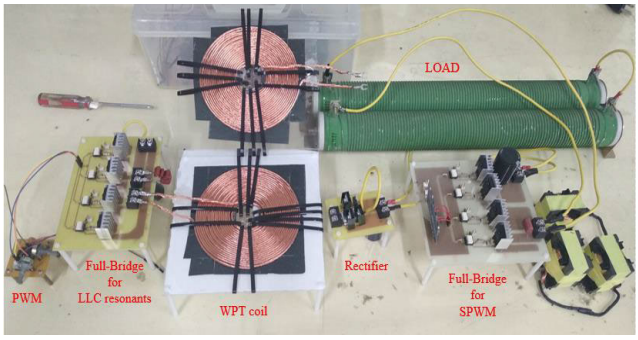

FIGURE 32. The prototype of the proposed circuits and WPTcoils.

the DC output mode function and the efficiency, the DC electronic load is placed to achieve the output power measurement. On the other hand, in order to verify and measure the AC output function, the wire-wound resistors (AC resistor load network) are combined for accomplishing AC output mode and the AC mode efficiency measurement. Table 3 lists all the testing equipment and the instruments for this study.

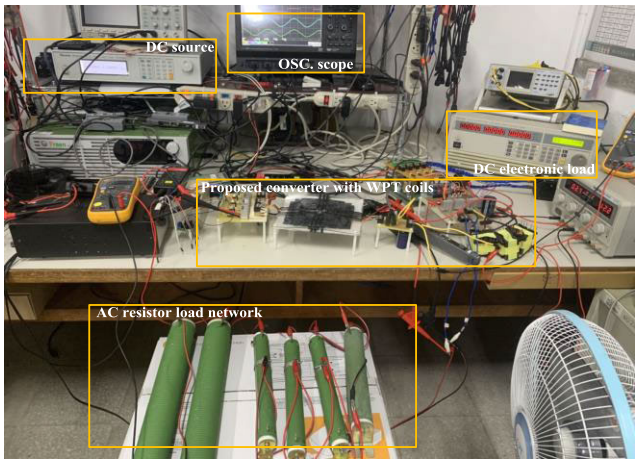

FIGURE 33. Testing environment and setup of the proposed scheme.

V. CONCLUSION

This paper focuses on a novel wireless power transfer scheme for providing an AC or DC output to specific load. For example, this novel scheme and the concept can be used for extending the application of an EV wireless charging station. If an EV has an on board charger (OBC) within, the wireless charging station can provide AC output power to the OBC then charges to the battery of EV. Conversely, if an EV has no on board charger, the wireless charging station can switch the output mode to DC for charging the battery of EV directly. Referred to the experimental results, the switches at the primary side have ZVS function for reducing switching losses effectively. Besides, the measurements and experimental waveforms prove that the proposed topology is feasible. The EV wireless charging equipment manufactures can extend the output standards for user's EV charging requirements and the specifications in the near future.

In addition, the proposed wireless power transfer topology gives a concept for AC or DC output mode selection. The series post-stage regulator at the output of the proposed WPT converter is necessary to meet the standard of EV batter systems or the specification of specific loads.

REFERENCES

[1] S. Cheon, Y.-H. Kim, S.-Y. Kang, M. L. Lee, J.-M. Lee, and T. Zyung, "Circuit-model-based analysis of a wireless energy-transfer system via coupled magnetic resonances," *IEEE Trans. Ind. Electron.*, vol. 58, no. 7, pp. 2906–2914, Jul. 2011.

[2] I. Mayordomo, T. Drager, P. Spies, J. Bernhard, and A. Pflaum, "An overview of technical challenges and advances of inductive wireless power transmission," *Proc. IEEE*, vol. 101, no. 6, pp. 1302–1311, Jun. 2013.

[3] J. Dai and D. C. Ludois, "A survey of wireless power transfer and a critical comparison of inductive and capacitive coupling for small gap applications," *IEEE Trans. Power Electron.*, vol. 30, no. 11, pp. 6017–6029, Nov. 2015.

[4] C. Shi, Y. Tang, and A. Khaligh, "A single-phase integrated onboard battery charger using propulsion system for plug-in electric vehicles," *IEEE Trans. Veh. Technol.*, vol. 66, no. 12, pp. 10899–10910, Dec. 2017.

[5] M. Nassary, M. Orabi, and M. Ghoneima, "Discussion of single-stage isolated unidirectional AC–DC on-board battery charger for electric vehicle," in *Proc. IEEE 4th Southern Power Electron. Conf. (SPEC)*, Dec. 2018, pp. 1–7.

[6] F. Musavi, W. Eberle, and W. G. Dunford, "A high-performance single-phase bridgeless interleaved PFC converter for plug-in hybrid electric vehicle battery chargers," *IEEE Trans. Ind. Appl.*, vol. 47, no. 4, pp. 1833–1843, Jul. 2011.

[7] M. Y. Metwly, M. S. Abdel-Majeed, A. S. Abdel-Khalik, R. A. Hamdy, M. S. Hamad, and S. Ahmed, "A review of integrated on-board EV battery chargers: Advanced topologies, recent developments and optimal selection of FSCW slot/pole combination," *IEEE Access*, vol. 8, pp. 85216–85242, 2020.

[8] L. Zhang, S. Chi, Q. Hu, K. Chen, and L. Lyu, "Reliability oriented modeling and analysis of PLC for EVs to charging piles communication system based on IPA-SAMP impulse noise cancelation," *IEEE Access*, vol. 8, pp. 4605–4614, 2020.

[9] J. Ma, W. An, W. Ming, J. Du, W. Yin, and J. Chen, "Coordinated control strategy for electric vehicle charging piles to prevent overload of distribution transformer," in *Proc. 5th Asia Conf. Power Electr. Eng. (ACPEE)*, Jun. 2020, pp. 684–688.

[10] S. A. Q. Mohammed and J.-W. Junga, "Comprehensive state-of-the-art review of wired/wireless charging technologies for battery electric vehicles: Classification/common topologies/future research issues," *IEEE Access*, vol. 9, pp. 19572–19585, 2021.

[11] M. Adil, J. Ali, Q. T. H. Ta, M. Attique, and T.-S. Chung, "A reliable sensor network infrastructure for electric vehicles to enable dynamic wireless charging based on machine learning technique," *IEEE Access*, vol. 8, pp. 187933–187947, 2020.

[12] A. Khaligh and S. Dusmez, "Comprehensive topological analysis of conductive and inductive charging solutions for plug-in electric vehicles," *IEEE Trans. Veh. Technol.*, vol. 61, no. 8, pp. 3475–3489, Oct. 2012.

[13] D. Kosmanos, L. A. Maglaras, M. Mavrovouniotis, S. Moschoyiannis, A. Argyriou, A. Maglaras, and H. Janicke, "Route optimization of electric vehicles based on dynamic wireless charging," *IEEE Access*, vol. 6, pp. 42551–42565, 2018.

[14] C. Li, T. Ding, X. Liu, and C. Huang, "An electric vehicle routing optimization model with hybrid plug-in and wireless charging systems," *IEEE Access*, vol. 6, pp. 27569–27578, 2018.

[15] D. H. Nguyen, "Electric vehicle—Wireless charging-discharging lane decentralized peer-to-peer energy trading," *IEEE Access*, vol. 8, pp. 179616–179625, 2020.

[16] X. Mou, D. T. Gladwin, R. Zhao, H. Sun, and Z. Yang, "Coil design for wireless vehicle-to-vehicle charging systems," *IEEE Access*, vol. 8, pp. 172723–172733, 2020.

[17] H. Li, Z. Zhang, S. Wang, J. Tang, X. Ren, and Q. Chen, "A 300-kHz 6.6-kW SiC bidirectional LLC onboard charger," *IEEE Trans. Ind. Electron.*, vol. 67, no. 2, pp. 1435–1445, Feb. 2020.

[18] Z. Fang, T. Cai, S. Duan, and C. Chen, "Optimal design methodology for LLC resonant converter in battery charging applications based on time-weighted average efficiency," *IEEE Trans. Power Electron.*, vol. 30, no. 10, pp. 5469–5483, Oct. 2015.

[19] D. S. Gautam, F. Musavi, W. Eberle, and W. G. Dunford, "A zero-voltage switching full-bridge DC–DC converter with capacitive output filter for plug-in hybrid electric vehicle battery charging," *IEEE Trans. Power Electron.*, vol. 28, no. 12, pp. 5728–5735, Dec. 2013.

[20] W. Haoyu, S. Dusmez, and A. Khaligh, "Design and analysis of a full-bridge LLC-based PEV charger optimized for wide battery voltage range," *IEEE Trans. Veh. Technol.*, vol. 63, no. 4, pp. 1603–1613, May 2014.

[21] H. F. Xiao, K. Lan, and L. Zhang, "A quasi-unipolar SPWM full-bridge transformerless PV grid-connected inverter with constant common-mode voltage," *IEEE Trans. Power Electron.*, vol. 30, no. 6, pp. 3122–3132, Jun. 2015.

[22] L. He and C. Cheng, "A bridge modular switched-capacitor-based multilevel inverter with optimized SPWM control method and enhanced power-decoupling ability," *IEEE Trans. Ind. Electron.*, vol. 65, no. 8, pp. 6140–6149, Aug. 2018.

[23] X. Sun, B. Wang, Y. Zhou, W. Wang, H. Du, and Z. Lu, "A single DC source cascaded seven-level inverter integrating switched-capacitor techniques," *IEEE Trans. Ind. Electron.*, vol. 63, no. 11, pp. 7184–7194, Nov. 2016.

[24] J. Liu, J. Zhang, T. Q. Zheng, and J. Yang, "A modified gain model and the corresponding design method for an LLC resonant converter," *IEEE Trans. Power Electron.*, vol. 32, no. 9, pp. 6716–6727, Sep. 2017.

[25] I. Demirel and B. Erkmen, "A very low-profile dual output LLC resonant converter for LCD/LED TV applications," *IEEE Trans. Power Electron.*, vol. 29, no. 7, pp. 3514–3524, Jul. 2014.
[26] Z. Hu, L. Wang, H. Wang, Y. F. Liu, and P. C. Sen, "An accurate design algorithm for LLC resonant converters—Part I," *IEEE Trans. Power Electron.*, vol. 31, no. 8, pp. 5435–5447, Aug. 2016.
[27] J. Deng, S. Li, S. Hu, C. C. Mi, and R. Ma, "Design methodology of LLC resonant converters for electric vehicle battery chargers," *IEEE Trans. Veh. Technol.*, vol. 63, no. 4, pp. 1581–1592, May 2014.
[28] H. Wang, M. Shang, and D. Shu, "Design considerations of efficiency enhanced LLC PEV charger using reconfigurable transformer," *IEEE Trans. Veh. Technol.*, vol. 68, no. 9, pp. 8642–8651, Sep. 2019.
[29] Y. Chen, J. Xu, J. Sha, L. Lin, and J. Cao, "An improved fundamental harmonic approximation to describe filter inductor influence on steady-state performance of parallel-type resonant converter," *IEEE Trans. Power Electron.*, vol. 34, no. 3, pp. 2467–2478, Mar. 2019.
[30] Y. Shen, W. Zhao, Z. Chen, and C. Cai, "Full-bridge LLC resonant converter with series-parallel connected transformers for electric vehicle on-board charger," *IEEE Access*, vol. 6, pp. 13490–13500, 2019.
[31] I. Iramnaaz, H. Schellevis, B. Rejaei, R. Fitch, and Y. Zhuang, "Self-biased low loss conductor featured with skin effect suppression for high quality RF passives," *IEEE Trans. Magn.*, vol. 48, no. 11, pp. 4139–4142, Nov. 2012.
[32] M. Yamaguchi, T. Yanai, H. Nakayama, R. Sai, H. Fujiwara, Y. Kitai, M. Sato, and U. Sangawa, "Skin effect suppressed Ni–Fe/Cu electroplated multilayer wiring for high data-rate and low delay-time I/O interface board," *IEEE Trans. Magn.*, vol. 54, no. 11, Nov. 2018, Art. no. 4002705.
[33] H. A. Wheeler, "Formulas for the skin effect," *Proc. IRE*, vol. 30, no. 9, pp. 412–424, Sep. 1942.

SEN-TUNG WU was born in Taipei, Taiwan, in 1980. He received the B.S., M.S., and Ph.D. degrees from the Department of Electronic and Computer Engineering, National Taiwan University of Science and Technology, Taiwan, in 2014. He had working experience in research and development department of switching power supply design manufacture for several years. He has been working as an Assistant Professor with the Department of Electrical Engineering, National Formosa University, Taiwan, since 2017. His main research interests include power electronics, energy converter designs, battery chargers, bidirectional converters, power factor correction circuit design, and wireless power transfer applications.

CHI-HSUAN HAN was born in Chiayi, Taiwan, in 1995. He received the B.S. and M.S. degrees from the Department of Electrical Engineering, National Formosa University, Yunlin, Taiwan, in 2019. He has been working at LITE-ON Technology Company, Taiwan, as an Research and Development Electrical Engineer, since 2020. His research interests include power electronics and wireless power transfer systems.